# Thermodynamic stability of LaMnO₃ and its competing oxides: A hybrid density functional study of an alkaline fuel cell catalyst

E. A. Ahmad,[1,2,*] L. Liborio,[1,2] D. Kramer,[1,3] G. Mallia,[1,2] A. R. Kucernak,[1] and N. M. Harrison[1,2,4]

[1]*Department of Chemistry, Imperial College London, South Kensington, London SW7 2AZ, United Kingdom*
[2]*Thomas Young Centre, Imperial College London, South Kensington, London SW7 2AZ, United Kingdom*
[3]*Faculty of Engineering and the Environment, University of Southampton, University Road, Southampton SO17 1BJ, United Kingdom*
[4]*Daresbury Laboratory, Daresbury, Warrington, WA4 4AD, United Kingdom*

The phase stability of LaMnO₃ with respect to its competing oxides is studied using hybrid-exchange density functional theory (DFT) as implemented in CRYSTAL09. The underpinning DFT total-energy calculations are embedded in a thermodynamic framework that takes optimal advantage of error cancellation within DFT. It has been found that by using the *ab initio* thermodynamic techniques described here, the standard Gibbs formation energies can be calculated to a significantly greater accuracy than was previously reported (a mean error of 1.6% with a maximum individual error of −3.0%). This is attributed to both the methodology for isolating the chemical potentials of the reference states, as well as the use of the Becke, three-parameter, Lee-Yang-Parr (B3LYP) functional to thoroughly investigate the ground-state energetics of the competing oxides.

PACS number(s): 88.30.ph, 31.15.A−, 81.30.−t

## I. INTRODUCTION

LaMnO₃ is well known as a perovskite material that can exhibit useful properties for magnetic sensors and solid oxide fuel cells (SOFCs).[1–3] A recent study has also revealed promising catalytic activity for LaMnO₃ in facilitating oxygen reduction in alkaline fuel cells (AFCs).[4] This presents a great opportunity for commercialization of AFC technology, since LaMnO₃ has a significant economic advantage over noble metals.

AFCs differ greatly from SOFCs, as they use a liquid electrolyte, usually KOH, and therefore operate in a significantly lower temperature range (25–70 °C).[5] This introduces a completely different environment, where the materials used for the catalysis of oxygen reduction on the cathode are expected to behave differently. LaMnO₃ has to be studied under these conditions to understand its bulk properties and corresponding surfaces. For this purpose, a complete picture of the thermodynamic stability of LaMnO₃ with respect to the competing oxides (La₂O₃, MnO₂, Mn₂O₃, Mn₃O₄, and MnO) is necessary.

LaMnO₃ has been studied extensively by experiment [with x-ray[6–11] and neutron diffraction,[7,12] scanning[10,11] and transmission electron microscopy,[10] electron paramagnetic resonance,[9] thermogravimetry (TG),[6,10,12,13] differential thermal analysis (DTA),[11,12] and differential scanning[6,8,10] and alternating current calorimetry[8]]. However, not much literature can be found that investigates the factors affecting the reactivity of LaMnO₃ as a catalyst in an AFC environment.[14] This is also true from a theoretical point of view, and although the electronic structure of the low-temperature orthorhombic phase of LaMnO₃ is well understood (by adopting unrestricted Hartree-Fock[15,16] and hybrid-exchange density functional theory[17,18]), there is a lack of knowledge of surface properties. Instead, the majority of such studies have been directed toward understanding the surface of the high-temperature cubic phase, with relevance to SOFC conditions.[19–23] Efforts to understand the thermodynamics and surface properties of orthorhombic LaMnO₃ can be found in recent literature,[24,25] but there

has been no comprehensive study of the thermodynamics of orthorhombic LaMnO₃ and its competing oxides.

Concerning the series of manganese oxides, there is a large number of papers which explore their properties, including efforts directly related to the thermodynamics. The heat capacity has been obtained by calorimetry, and the thermal stability and phase transitions have been analyzed by TG, differential TG, and DTA.[26–29] Quantum mechanical simulations have been performed to study the formation energies of this series by adopting different density functionals [Perdew and Wang 1991 (PW91),[25] and Perdew-Burke-Ernzerhof (PBE), PBE + U (in which an empirical on-site repulsive potential is added), PBE0 (in which 25% of the PBE exchange potential is replaced by non-local Fock exchange), and Heyd-Scuseria-Ernzerhof (HSE) (Ref. 30)]. The energetics of these compounds are characterized by a strong interplay between geometry and electronic structure, thus requiring an accurate treatment of exchange and correlation for the description of the electron localization. This is especially important if one is to obtain a consistent set of formation energies, as Mn adopts different valence states within the series. Previously calculated formation energies are affected by a significant error relative to experiment: the mean error is in the range of (7–22)%.[25,30] Apart from the inaccuracy of generalized-gradient approximation (GGA) -type functionals regarding the energetics of correlated systems, this can also be attributed to the methodology adopted to calculate the chemical potential of Mn and O, as pointed out in Sec. IV B. A proper estimation of the formation energies of the various competing compounds is crucial to build the phase diagram. Even small energetic inaccuracies can paint a different picture of phase stability in the La-Mn-O system, as demonstrated in Sec. IV C. Therefore, it is worth pointing out that no previous first-principles study to our knowledge has been able to provide an accurate representation of the stability regions of LaMnO₃ with respect to all of the competing oxides.

The aim of this study is to calculate the bulk phase diagram of the La-Mn-O system and to outline a suitable methodology for the study of the thermodynamics of the compounds in

this multivalent series. In addition, an investigation of the ground state of the compounds with regard to their geometry and magnetic state is performed. The Becke, three-parameter, Lee-Yang-Parr (B3LYP) hybrid-exchange density functional has been adopted, since it is well documented that it provides an accurate description of the electronic structure of localized and correlated systems (particularly for transition metal oxides).[17,31–40] The paper is organized as follows: in Sec. II the methodology is outlined, in Sec. III the computational details are provided, in Sec. IV the results are discussed, and conclusions are drawn in Sec. V.

## II. METHODOLOGY

In this section, the methodology used to construct the phase diagram is described. This relies on the calculation of the Gibbs formation energies $\Delta G_f^0$ of all of the involved compounds. This in turn requires the determination of the standard chemical potentials of the elements, $\mu^0$.

We will generally neglect entropic and volumetric work contributions to the Gibbs energy and approximate $G$ with the total energy $E$ at $0\,K$ as given by density functional theory (DFT). This is well justified for solids in the temperature and pressure range of interest, because the entropic contribution is mainly vibrational and the volume of solids is nearly independent of pressure and temperature. Hence, these terms are small and tend to cancel.[40] The reference state for oxygen, however, is the gaseous dimer and needs further consideration. The Gibbs energy of an (ideal) gas contains significant translational and rotational entropy as well as volumetric work.

The following expression for the oxygen chemical potential as a function of of $p_{O_2}$ and $T$ reflects this:[41]

$$\mu_{O_2}(p_{O_2}, T) = E_0 + (\mu_{O_2}^0 - E_0)\frac{T}{T^0} - \frac{5k_B}{2}T \ln\left(\frac{T}{T^0}\right)$$
$$+ k_B T \ln\left(\frac{p_{O_2}}{p_{O_2}^0}\right). \qquad (1)$$

This expression contains two unknown quantities: $E_0$, the energy per $O_2$ molecule at 0 K, and $\mu_{O_2}^0$, the chemical potential of an $O_2$ molecule at standard conditions (where the superscript 0 indicates standard conditions: $T^0 = 298.15$ K and $p_{O_2}^0 = 1$ bar). $E_0$ can be reliably calculated using the B3LYP functional with DFT as outlined in Sec. III, while $\mu_{O_2}^0$ is normally estimated using experimental data. Since we need $\mu_{O_2}^0$ rather than $\mu_{O_2}(p_{O_2}, T)$ to calculate the Gibbs formation energies, it is useful to adapt this expression for this purpose. To do so, it is necessary to introduce the Shomate equation, which expresses the temperature dependence of the Gibbs free energies per mole at standard pressure (i.e., $p_{O_2} = p_{O_2}^0$):

$$\mu_{O_2}^0(t) = \mu_{O_2}^0 + t^0 S^0 + A[t - t\ln(t)] - B\frac{t^2}{2} - C\frac{t^3}{6}$$
$$- D\frac{t^4}{12} - E\frac{1}{2t} + F - Gt - H, \qquad (2)$$

where $t = T/1000$ and the coefficients are given in Table I. By equating the temperature derivatives of Eqs. (1) and (2) at

TABLE I. The parameters for the range 100–700 K (Ref. 42).

| | | |
|---|---|---|
| $A$ | $31.32234 \times 10^3$ | kJ/(mol K) |
| $B$ | $-20.23531 \times 10^6$ | kJ/(mol K²) |
| $C$ | $57.86644 \times 10^9$ | kJ/(mol K³) |
| $D$ | $-36.50624 \times 10^{12}$ | kJ/(mol K⁴) |
| $E$ | $-0.007374 \times 10^{-3}$ | kJ K/mol |
| $F$ | $-8.903471$ | kJ/mol |
| $G$ | $246.7945$ | kJ/mol |
| $H$ | $0$ | kJ/mol |

$p_{O_2} = p_{O_2}^0$, $\mu_{O_2}^0(T)$ is obtained:

$$\mu_{O_2}^0(T) = E_0 + T^0\left[\frac{5k_B}{2}\ln\left(\frac{T}{T^0}\right) + \frac{5k_B}{2} + \frac{1}{1000}\right.$$
$$\left. \times\left(-A\ln(t) - Bt - \frac{1}{2}Ct^2 - \frac{1}{3}Dt^3 + \frac{E}{2t^2} - G\right)\right], \qquad (3)$$

which relies on only one unknown quantity $E_0$ and gives us $\mu_{O_2}^0$ when $T = T^0$. Instead of relying on DFT to provide energetics for the metallic reference states of La and Mn, we adopt an approach where the chemical potential of La and Mn in their standard states is obtained using the Gibbs formation energy of their oxides. This is suitable for calculations involving the use of the B3LYP functional, since it contains exact Fock exchange, and therefore provides a poor approximation for metals. The general formula for the formation energies of these oxides is

$$\Delta G_{fM_xO_y}^0 = \mu_{M_xO_y}^{\text{bulk}} - x\mu_M^0 - y\mu_O^0, \qquad (4)$$

where $M$ and O are metal and oxygen in the oxide $M_xO_y$, $\Delta G_{fM_xO_y}^0$ is the standard Gibbs formation energy from experiment,[43] and $\mu_{M_xO_y}^{\text{bulk}}$ is the chemical potential (Gibbs energy) of the bulk oxide. In the case of La, $\mu_{La}^0$ is calculated by introducing the value of $\mu_{O_2}^0$ given by the previous method into the equation,

$$\Delta G_{fLa_2O_3}^0 = \mu_{La_2O_3}^{\text{bulk}} - 2\mu_{La}^0 - \frac{3}{2}\mu_{O_2}^0, \qquad (5)$$

where the potential for the bulk $La_2O_3$, $\mu_{La_2O_3}^{\text{bulk}}$, can be equated to the ground-state energy, as discussed previously.[40] In the case of the manganese oxides the same approach can be applied; however, since there are several oxides, slightly different manganese chemical potentials arise. These values have to be averaged to provide a value to calculate the *ab initio* formation energies of the manganese oxides and LaMnO₃. A standard deviation 0.10 eV in the set of values was obtained, indicating a good approximation of the energetics of the Mn oxides. A lower deviation is limited by the accuracy of the obtained ground states (i.e., the noncollinear magnetism of Mn₃O₄; see Sec. IV A) and due to the fact that there is a large difference in the valence states of manganese in its oxides.

The quantities $\mu_{La}^0$, $\mu_{Mn}^0$, and $\mu_{O_2}^0$ define the upper stability limits in terms of the chemical potentials $\mu_{La}$, $\mu_{Mn}$, and $\mu_{O_2}$ for any compound in the system. Therefore it is true that

$$\mu_i - \mu_i^0 \leqslant 0, \qquad (6)$$

where $i = \mathrm{La,Mn,O}$. Above these limits the compounds decompose into their constituent elements. These conditions can be used to introduce a change of variable $\Delta\mu_i = \mu_i - \mu_i^0$ to give

$$\Delta\mu_i \leqslant 0, \tag{7}$$

which is convenient for the construction of a phase diagram. For example, the equilibrium chemical potential of LaMnO₃ with respect to its elements, given by

$$\mu_{\mathrm{La}} + \mu_{\mathrm{Mn}} + \tfrac{3}{2}\mu_{\mathrm{O}_2} = \mu_{\mathrm{LaMnO_3}}^{\mathrm{bulk}}, \tag{8}$$

can be expressed as

$$\Delta\mu_{\mathrm{La}} + \Delta\mu_{\mathrm{Mn}} + \tfrac{3}{2}\Delta\mu_{\mathrm{O}_2} = \Delta G_{f\mathrm{LaMnO_3}}^0, \tag{9}$$

by stoichiometrically subtracting $\mu_{\mathrm{La}}^0$, $\mu_{\mathrm{Mn}}^0$, and $\mu_{\mathrm{O}_2}^0$ from both sides of Eq. (8). Note that the stoichiometrically weighted chemical potentials $\Delta\mu_{\mathrm{La}}^0$, $\Delta\mu_{\mathrm{Mn}}^0$, and $\Delta\mu_{\mathrm{O}_2}^0$ must sum to $\Delta G_{f\mathrm{LaMnO_3}}^0$. Hence, as has been pointed out previously,[44] $\Delta\mu_i$ for each element is not allowed to become so negative (i.e., more negative than $\Delta G_{f\mathrm{LaMnO_3}}^0$) that the others break their upper limit $\Delta\mu_i \leqslant 0$. Therefore, in the case of LaMnO₃, the lower limits for the chemical potentials $\mu_i$ are defined as

$$\Delta\mu_i \geqslant \frac{1}{x_i}\Delta G_{f\mathrm{LaMnO_3}}^0, \tag{10}$$

with $x_i$ equal to the stoichiometric coefficient of $i$. When Eqs. (7) and (10) are combined, it follows that

$$\frac{1}{x_i}\Delta G_{f\mathrm{LaMnO_3}}^0 \leqslant \Delta\mu_i \leqslant 0. \tag{11}$$

By considering Eq. (9) and the limits that have been discussed, a region in the La-Mn-O chemical potential space can now be defined where LaMnO₃ is stable with respect to the reference states. The competing phases, however, impose similar conditions and further limit the range of chemical potentials for which LaMnO₃ is stable. Accordingly, a phase diagram can be constructed to show the stability region for LaMnO₃ by considering the equivalent equations for each of the competing oxides.

### III. COMPUTATIONAL DETAILS

All calculations have been performed using the CRYSTAL09 software package,[45] based on the expansion of the crystalline orbitals as a linear combination of a local basis set (BS) consisting of atom-centered Gaussian orbitals. The Mn and O atoms are described by a triple-valence all-electron BS: an 86-411$d$(41) contraction (one $s$, four $sp$, and two $d$ shells) and an 8-411$d$(1) contraction (one $s$, three $sp$, and one $d$ shells), respectively; the most diffuse $sp(d)$ exponents are $\alpha^{\mathrm{Mn}} = 0.4986(0.249)$ and $\alpha^{\mathrm{O}} = 0.1843(0.6)$ bohrs$^{-2}$.[46] The La basis set includes a nonrelativistic pseudopotential to describe the core electrons, while the valence part consists of a 411$p$(411)$d$(311) contraction scheme (with three $s$, three $p$, and three $d$ shells); the most diffuse exponent is $\alpha^{\mathrm{La}} = 0.15$ bohrs$^{-2}$ for each $s$, $p$, and $d$.[17]

Electron exchange and correlation are approximated using the B3LYP hybrid-exchange functional, which, as noted above, is expected to be more reliable than the local density approximation or GGA approaches.[31,34,47] The exchange and correlation potentials and energy functional are integrated numerically on an atom-centered grid of points. The integration over radial and angular coordinates is performed using Gauss-Legendre and Lebedev schemes, respectively. A pruned grid consisting of 99 radial points and 5 subintervals with (146,302,590,1454,590) angular points has been used for all calculations [the XXLGRID option implemented in CRYSTAL09 (Ref. 45)]. This grid converges the integrated charge density to an accuracy of about $\times 10^{-6}$ electrons per unit cell. The Coulomb and exchange series are summed directly and truncated using overlap criteria with thresholds of $10^{-7}$, $10^{-7}$, $10^{-7}$, $10^{-7}$, and $10^{-14}$ as described previously.[45,48] Reciprocal space sampling was performed on a Pack-Monkhorst net with a shrinking factor of 8 for all cells except the larger cell of orthorhombic Mn₂O₃, for which a shrinking factor of 4 was used. The self-consistent field procedure was converged up to a tolerance in the total energy of $\Delta E = 1 \times 10^{-7} E_h$ per unit cell.

The cell parameters and the internal coordinates were determined by minimization of the total energy within an iterative procedure based on the total-energy gradient calculated analytically with respect to the cell parameters and nuclear coordinates. Convergence was determined from the root mean square (rms) and the absolute value of the largest component of the forces. The thresholds for the maximum and the rms forces (the maximum and the rms atomic displacements) were set to 0.000 45 and 0.000 30 (0.001 80 and 0.0012) in atomic units. Geometry optimization was terminated when all four conditions were satisfied simultaneously.

### IV. RESULTS

#### A. Geometries and energetics

The optimized lattice parameters of the most stable (crystallographic and magnetic) phases for LaMnO₃ and the competing oxides are given in Table II. For the competing oxides some of the other commonly observed crystallographic phases and magnetic configurations have been investigated and the results are reported in Table III. The $\Delta E$ (meV per formula unit) is the increase in energy from the most stable phase and magnetic configuration of the corresponding compound given in Table II.

Only the low-temperature phase of LaMnO₃, which is orthorhombic and $A$-type antiferromagnetic,[18,49,60] has been simulated. The calculated lattice parameters **b** and **c** are in good agreement with the experimental values; the percentage error is less than 1.5%. The **a** parameter, however, is overestimated by almost 5% with respect to the low-temperature (9 K) structure cited. It is noted that there is no experimental certainty for this parameter; values between 5.472 and 5.748 Å are reported.[50] Only two sets of values based on theory have been reported previously. In one case, the unrestricted Hartree-Fock level of theory is used [**a** = 5.740, **b** = 7.754, **c** = 5.620 (Ref. 16)], while the GGA to DFT is adopted in the other [**a** = 5.7531, **b** = 7.7214, **c** = 5.5587 (Ref. 24)]; both predict a value of **a** close to the upper limit observed experimentally.

The only competing binary oxide containing La is La₂O₃, which occurs in a body-centered cubic structure for the most

TABLE II. Experimental and optimized lattice parameters (**a**, **b**, and **c** in Å) of the most stable (crystallographic and magnetic) phases at low temperature for $LaMnO_3$ and the competing oxides. The magnetic solution is indicated in the second column as AFM, FM, and NM for the antiferromagnetic, ferromagnetic, and nonmagnetic cases; the type of AFM is labeled by ($A$) and ($G$); see Ref. 49. The arrows following the type of magnetic phase indicate the spin direction of the sequence of Mn atoms in the cell according to Fig. 1. The temperature at which the experimental geometry was obtained is given in the column labeled $T$ (K) according to the references provided and Ref. 50; a specified range indicates where the compound is stable. The percentage errors (%) of the calculated lattice parameters relative to the experimental parameters cited for the compound are also included in italics.

| Compound | | | Space group | | **a** | **b** | **c** | $T$ (K) | Reference |
|---|---|---|---|---|---|---|---|---|---|
| $LaMnO_3$ | | Expt. | *Pnma* | (62) | 5.730 | 7.672 | 5.536 | 9 | 51 |
| | AFM (*A*) | Opt. | | | 6.010 | 7.735 | 5.614 | | |
| | | | | | *4.89* | *0.82* | *1.41* | | |
| $La_2O_3$ | | Expt. | *Ia*3 | (206) | 11.360 | | | $\leqslant$770 | 52 |
| | NM | Opt. | | | 11.583 | | | | |
| | | | | | *1.96* | | | | |
| $MnO_2$ | | Expt. | *Pnma* | (62) | 9.273 | 2.864 | 4.522 | 298 | 53 |
| | AFM ↑↓↑↓ | Opt. | | | 9.269 | 2.882 | 4.624 | | |
| | | | | | *−0.04* | *0.62* | *2.26* | | |
| $Mn_2O_3$ | | Expt. | *Pbca* | (61) | 9.416 | 9.423 | 9.405 | $\leqslant$302 | 54 |
| | FM | Opt. | | | 9.479 | 9.538 | 9.566 | | |
| | | | | | *0.67* | *1.22* | *1.71* | | |
| $Mn_3O_4$ | | Expt. | *I*41/*amd* | (141) | 5.757 | | 9.424 | 10 | 55 |
| | FiM ↑↑↓↓↑↑ | Opt. | | | 5.814 | | 9.558 | | |
| | | | | | *0.99* | | *1.42* | | |
| MnO | | Expt. | *Fm*3*m* | (225) | 4.444 | | | 293 | 56 |
| | AFM (*G*) | Opt. | | | 4.458 | | | | |
| | | | | | *0.32* | | | | |

stable phase (see Table II) and in the trigonal structure at high temperature (see Table III);[50,52,61] both are nonmagnetic.

The competing binary Mn oxides are discussed in terms of oxidation state as follows: $MnO_2$(IV), $Mn_2O_3$(III),

TABLE III. Experimental and optimized lattice parameters of some of the other commonly observed structures. Annotation is the same as in Table II, with the addition of $\Delta E$ (meV per formula unit), which is the increase in energy from the most stable geometry and magnetic configuration of the corresponding compound given in Table II. * indicates the temperature at which the sample was synthesized.

| Compound | | | Space group | | **a** | **b** | **c** | $\Delta E$ | $T$ (K) | Reference |
|---|---|---|---|---|---|---|---|---|---|---|
| $La_2O_3$ | | Expt. | $P\bar{3}m1$ | (164) | 3.937 | | 6.129 | | $\geqslant$770 | 52 |
| | NM | Opt. | | | 3.999 | | 6.331 | 136 | | |
| $MnO_2$ | | Expt. | *Pnma* | (62) | 9.273 | 2.864 | 4.522 | | 298 | 53 |
| | FM | Opt. | | | 9.199 | 2.885 | 4.674 | 43 | | |
| | AFM ↑↓↓↑ | Opt. | | | 9.264 | 2.880 | 4.627 | 8 | | |
| | AFM ↓↓↑↑ | Opt. | | | 9.202 | 2.886 | 4.677 | 39 | | |
| | | Expt. | *P*42/*mnm* | (136) | 4.404 | | 2.877 | | | 57 |
| | FM | Opt. | | | 4.441 | | 2.895 | 67 | | |
| | AFM | Opt. | | | 4.429 | | 2.894 | 31 | | |
| $Mn_2O_3$ | | Expt. | *Ia*3 | (206) | 9.417 | | | | 723 | 58 |
| | FM | Opt. | | | 9.520 | | | 249 | | |
| $Mn_3O_4$ | | Expt. | *I*41/*amd* | (141) | 5.757 | | 9.424 | | 10 | 55 |
| | FM | Opt. | | | 5.842 | | 9.560 | 200 | | |
| | FiM ↑↑↓↓↓↓ | Opt. | | | 5.800 | | 9.577 | 12 | | |
| | FiM ↑↓↑↑↑↑ | Opt. | | | 5.822 | | 9.554 | 99 | | |
| | FiM ↑↑↑↓↑↓ | Opt. | | | 5.809 | 5.825 | 9.566 | 94 | | |
| | FiM ↑↑↑↓↑↑ | Opt. | | | 5.821 | 5.832 | 9.558 | 100 | | |
| | FiM ↑↓↑↓↑↓ | Opt. | | | 5.818 | | 9.554 | 82 | | |
| | | Expt. | *Pbcm* | (57) | 3.026 | 9.769 | 9.568 | | 1000* | 59 |
| | FM | Opt. | | | 3.069 | 9.977 | 9.637 | 770 | | |
| MnO | | Expt. | *Fm*3*m* | (225) | 4.444 | | | | 293 | 56 |
| | FM | Opt. | | | 4.483 | | | 96 | | |

$Mn_2O_3$



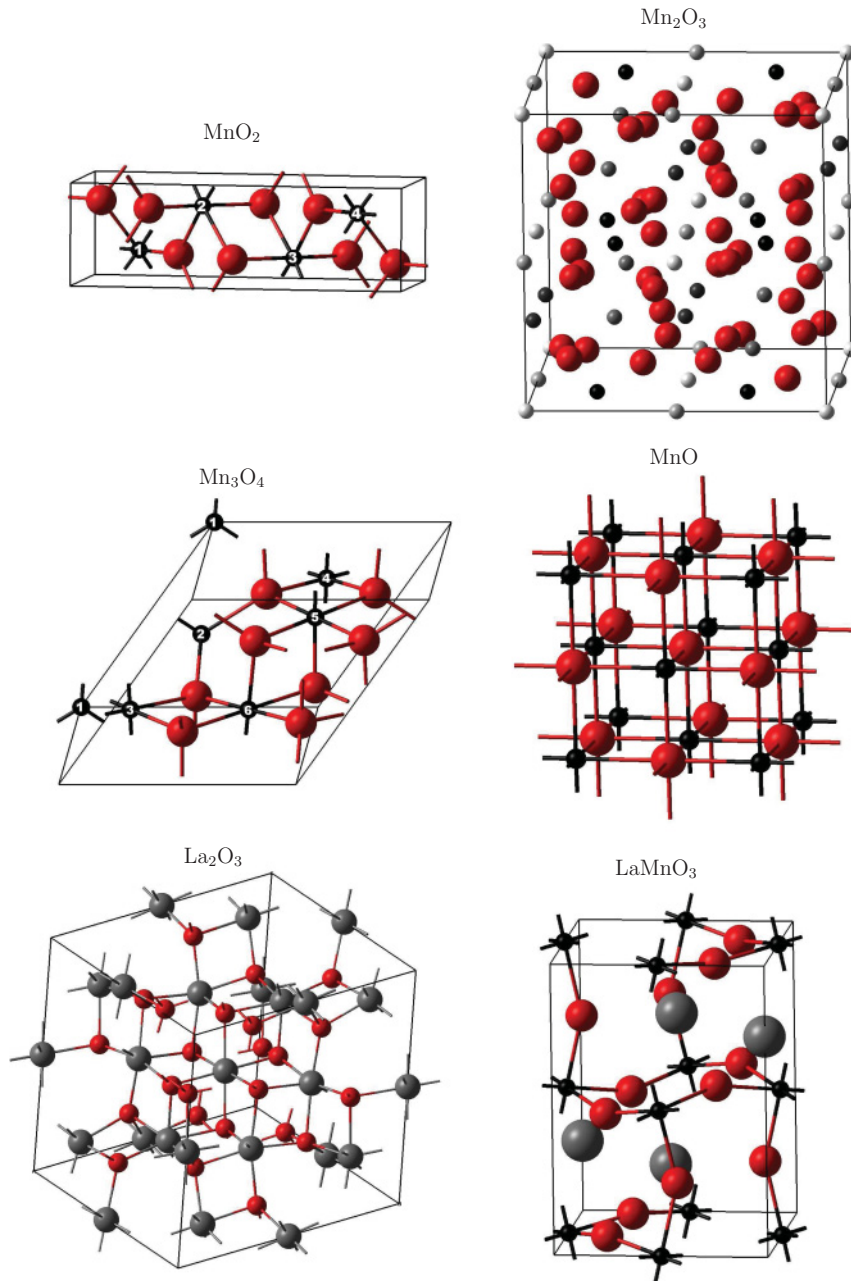$MnO_2$



$Mn_3O_4$



$MnO$



FIG. 1. (Color online) The crystallographic cell for $LaMnO_3$ and the competing oxides in the geometries indicated in Table II. Large, medium, and small spheres correspond to the La, O, and Mn atoms, respectively. In the case of $MnO_2$ and $Mn_3O_4$, the labeling of the Mn atoms is linked to the assignment of spin in Tables II and III. Symmetry-irreducible Mn atoms are given in gray-scale color for $Mn_2O_3$ for clarity.

$La_2O_3$



$LaMnO_3$



$Mn_3O_4(II/III)$, and MnO(II). For the manganese oxides in Table II the percentage error between the experimental and calculated lattice parameters is less than 2.3%.[34]

The lowest energy for $MnO_2$ was found for the orthorhombic (ramsdellite) antiferromagnetic structure, with the spin configuration as indicated by the arrows in Table II. The differences in energy between various spin configurations both within and between the orthorhombic and rutile (pyrolusite) structures are of the order of tens of meV. This can be linked to the high number of polymorphs observed for this material.[62,63] This finding is in agreement with previous work, but it has to be noted that the stability order is reversed when paramagnetic energies are obtained by fitting a Heisenberg Hamiltonian.[63] In fact, the rutile structure is reported to have a lower energy (by 22 meV) than the orthorhombic one.[63]

$Mn_2O_3$ was simulated in its cubic and orthorhombic forms. The relative energies agree with experiment, where the orthorhombic structure is considered stable at low temperature.[54,58] The structure was simulated only in its ferromagnetic form as there is no consensus yet on its low-temperature magnetic structure from experiment.[64,65]

Although $Mn_3O_4$ has a noncollinear magnetic structure with long-range ordering,[66,67] the simulation has been limited to ferromagnetic and ferrimagnetic (FiM) configurations that can be defined within the primitive cell, consistent with previous work.[30] The spinel FiM ↑↑↓↓↑↑ configuration (see Fig. 1 for notation) is the most stable. In Table III the various FiM and FM configurations of the spinel $Mn_3O_4$ are shown, differing within a range of 200 meV, while the high-pressure orthorhombic phase is drastically less stable ($\Delta E = 770$ meV).

TABLE IV. Gibbs free energy of formation (eV) for LaMnO$_3$ and the manganese oxides (Refs. 43 and 71).

| Compound | Experimental $\Delta G_f^0$ | Calculated $\Delta G_f^0$ | Error (%) |
|---|---|---|---|
| LaMnO$_3$ | −14.03 | −13.89 | −1.0 |
| MnO$_2$ | −4.82 | −4.68 | −3.0 |
| Mn$_2$O$_3$ | −9.13 | −9.21 | 0.9 |
| Mn$_3$O$_4$ | −13.30 | −13.61 | 2.4 |
| MnO | −3.76 | −3.76 | <0.1 |

MnO has a face-centered cubic *G*-type antiferromagnetic structure at low temperature ($T_N = 118$ K); the spins order ferromagnetically on (111) planes with antiferromagnetic coupling between neighboring planes.[68,69] The optimized structure is characterized by a uniform distortion of the cell angles by 1.52%, indicating that at low temperatures the unit cell of MnO becomes rhombohedrally distorted, in agreement with Hartree-Fock calculations[70] and neutron diffraction studies.[69] In addition, the distance between antiferromagnetically coupled Mn is shorter (3.135 Å) compared to the ferromagnetically coupled Mn (3.170 Å); therefore, a contraction occurs normal to the ferromagnetic (111) planes corresponding to a magnetostriction effect. This does not occur in the FM phase, which has an energy 96 meV higher and a Mn-Mn distance of 3.170 Å.

### B. Gibbs formation energies

The calculated Gibbs formation energies for the stable (lowest-energy) phases of LaMnO$_3$ and the competing Mn oxides are compared in Table IV with experimental Gibbs formation energies obtained from a thermochemical database.[43] The calculated and experimental $\Delta G_f^0$ are identical by construction for La$_2$O$_3$ (see Sec. II), and therefore it is omitted from this table.

The maximum percentage error of $\Delta G_f^0$ relative to the experimental value in Table IV does not exceed $\pm 3\%$; a positive (negative) error means that the Gibbs formation energy is underestimated (overestimated). The mean relative error is 1.6%. The atypically large error for MnO$_2$ is noteworthy. It can

be attributed to the natural occurance of Ruetschi defects in ramsdellite (orthorhombic MnO$_2$);[63] this can stabilize the experimental energies with respect to the (defect-free) calculated energy, because low-energy defects introduce configurational entropy and lower the Gibbs energy.

In general, the calculated formation energies of the manganese oxides are in very good agreement with experiment. This highlights the quality of the hybrid-exchange functional B3LYP, which is able to consistently describe the oxygen molecule and the complete set of manganese oxides, even though they are characterized by different oxidation states of the transition metal. The accuracy of the data in Table IV is a significant improvement on that present in recent reports [which have a mean error in the range of (7–22)%].[25,30] This larger error can be attributed partially to the functionals used (PW91, PBE, PBE + $U$, PBE0, and HSE) and partially to the approaches adopted for the approximations of $\mu_{Mn}^0$ and $\mu_{O_2}^0$, which did not adequately account for limited error cancellation in the respective approximations to DFT. Careful consideration of error cancellation can lead to significant improvements, as has been demonstrated in previous work.[72] However, errors have to be expected when $\mu_{Mn}^0$ and $\mu_{O_2}^0$ are approximated by using the *ab initio* energy of the metal and the oxygen molecule indiscriminately with respect to the exchange-correlation functional.

### C. Phase diagram

Phase diagrams, constructed from the experimental and calculated Gibbs formation energies, are compared in Fig. 2. The calculated bulk LaMnO$_3$ stability region is in good agreement with experiment. It is noted that in Fig. 2 the stability region of LaMnO$_3$ is affected by even a small percentage deviation from the experimental $\Delta G_f^0$ of LaMnO$_3$ and Mn$_3$O$_4$ (1% and 2.4%, respectively). However, from the previous studies,[25,30] the set of calculations with the greatest accuracy had a mean error of 7%, which includes a deviation of 16% for MnO$_2$.

Figure 3 shows the phase diagram in 3D space by inclusion of the $\Delta \mu_{La}^0$ axis. This allows for a better understanding of the stability of each compound and limiting phase equilibria. The
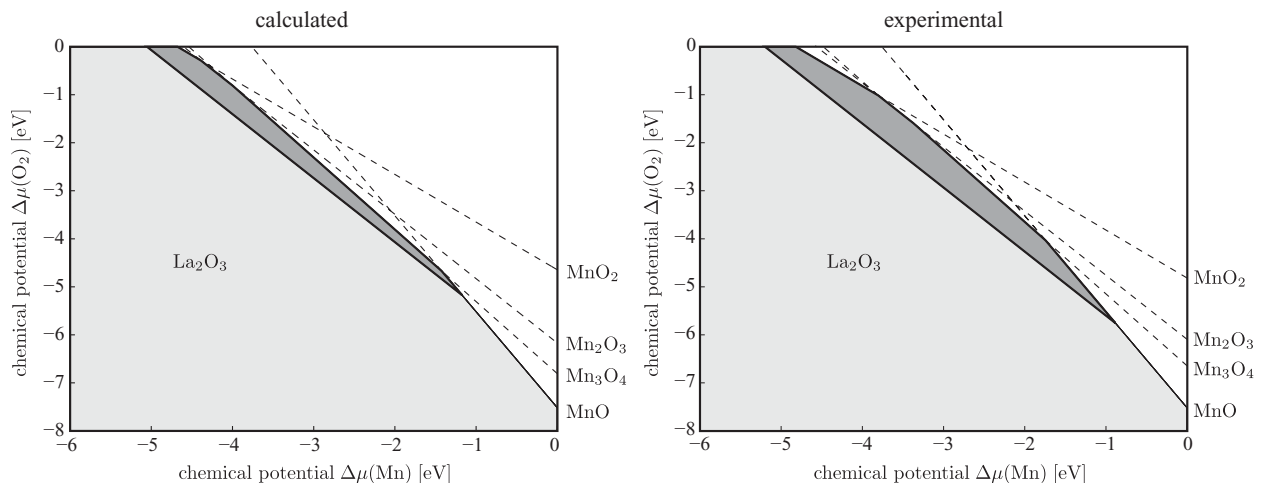


FIG. 2. Two-dimensional phase diagrams obtained by using the experimental and calculated Gibbs formation energy at standard conditions. The stability region of LaMnO$_3$ is represented by the dark gray area.
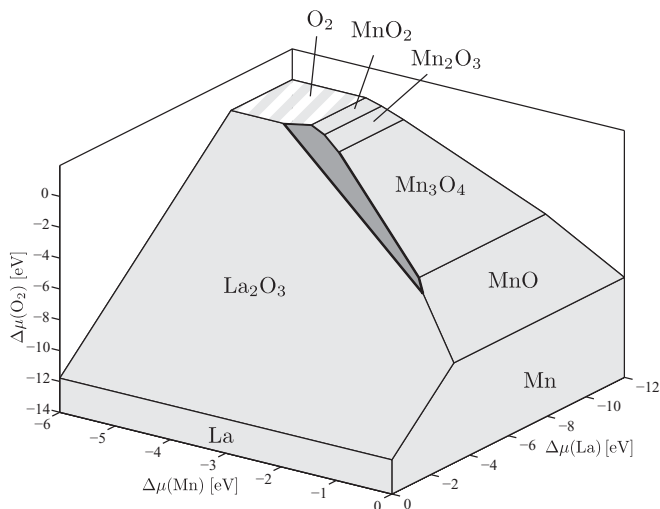
FIG. 3. Three-dimensional phase diagram constructed from the calculated Gibbs formation energies at standard conditions. The stability region of LaMnO₃ is represented by the dark gray area.

decomposition of LaMnO₃ into La₂O₃ and gaseous oxygen sets the lower limit of the chemical potential of manganese. On the other hand, the upper limit for the manganese chemical potential varies strongly according to the environment. In strongly oxidizing environments, the stability of LaMnO₃ is limited by the manganese oxide that can stabilize the most oxygen (MnO₂), while the reverse is true for a strongly reducing environment (MnO). Under mildly reducing or oxidizing conditions, LaMnO₃ forms equilibria with Mn₃O₄ and Mn₂O₃, which contain the intermediate (III) oxidation state of manganese.

Finally, the LaMnO₃ bulk stability region sets meaningful limits of the chemical potentials for the investigation of surface terminations, which is a prerequisite for the investigation of catalytic properties in relation to AFC applications.

## V. CONCLUSIONS

The thermodynamic phase stability of bulk LaMnO₃ and the manganese oxides has been investigated using hybrid DFT with periodic boundary conditions. The most stable geometric and magnetic phases of the compounds in the La-Mn-O system were determined and used to calculate the Gibbs formation energies. Quantitative agreement between calculated and

experimental formation energies at standard temperature and pressure was achieved (a mean error of 1.6%). This allowed us to investigate the different phase equilibria that confine the stability region of bulk LaMnO₃ in chemical potential space, and therefore the region where any surfaces of LaMnO₃ can be stable, for the complete system where metals, oxides, and gases exist.

The methodology developed was key to this investigation, as it allowed for the accurate calculation of the oxygen and manganese chemical potentials, and subsequently demonstrated that DFT simulations using the B3LYP functional can accurately predict the thermodynamics for the range of different valence states of manganese in its oxides. With regard to the study of LaMnO₃ as a catalyst in AFCs, this is crucial, as the surfaces of LaMnO₃ are certain to contain multiple oxidation states of manganese. In conclusion, our methodology properly described the thermodynamics of bulk LaMnO₃ and will be suitable for studies of its surface composition and structure.

*ehsan.ahmad08@imperial.ac.uk

[1] S. Jin, T. H. Tiefel, M. McCormack, R. A. Fastnacht, R. Ramesh, and L. H. Chen, Science **264**, 413 (1994).

[2] S. Tao, J. Irvine, and J. Kilner, Adv. Mater. **17**, 1734 (2005).

[3] T. Ishihara, *Perovskite Oxide for Solid Oxide Fuel Cells* (Springer, Berlin, 2009).

[4] M. Hayashi, H. Uemura, K. Shimanoe, N. Miura, and N. Yamazoe, J. Electrochem. Soc. **151**, A158 (2004).

[5] F. Bidault, D. Brett, P. Middleton, and N. Brandon, J. Power Sources **187**, 39 (2009).

[6] J. A. M. V. Roosmalen, E. H. P. Cordfunke, R. B. Helmholdt, and H. W. Zandbergen, J. Solid State Chem. **110**, 100 (1994).

[7] P. Norby, I. G. K. Andersen, E. K. Andersen, and N. H. Andersen, J. Solid State Chem. **119**, 191 (1995).

[8] H. Satoh, M. Takagi, K. ichi Kinukawa, and N. Kamegashira, Thermochim. Acta **299**, 123 (1997).

[9] C. Oliva and L. Forni, Catal. Commun. **1**, 5 (2000).

[10] D. S. Jung, S. K. Hong, and Y. C. Kang, J. Ceram. Soc. Jpn. **116**, 141 (2008).

[11] Y. Shimizu and T. Murata, J. Am. Ceram. Soc. **80**, 2702 (1997).

[12] J. Rodríguez-Carvajal, M. Hennion, F. Moussa, A. H. Moudden, L. Pinsard, and A. Revcolevschi, Phys. Rev. B **57**, R3189 (1998).

[13] K. Kitayama, J. Solid State Chem. **153**, 336 (2000).

[14] R. Singh, M. Malviya, Anindita, A. Sinha, and P. Chartier, Electrochim. Acta **52**, 4264 (2007).

[15] Y.-S. Su, T. A. Kaplan, S. D. Mahanti, and J. F. Harrison, Phys. Rev. B **61**, 1324 (2000).

[16] M. Nicastro and C. H. Patterson, Phys. Rev. B **65**, 205111 (2002).

[17] D. Muñoz, N. M. Harrison, and F. Illas, Phys. Rev. B **69**, 085115 (2004).

[18] S. Piskunov, E. Spohr, T. Jacob, E. A. Kotomin, and D. E. Ellis, Phys. Rev. B **76**, 012410 (2007).

[19] R. A. Evarestov, E. A. Kotomin, D. Fuks, J. Felsteiner, and J. Maier, Appl. Surf. Sci. **238**, 457 (2004).

[20] S. Piskunov, E. Heifets, T. Jacob, E. A. Kotomin, D. E. Ellis, and E. Spohr, Phys. Rev. B **78**, 121406 (2008).

[21] Y. Choi, D. S. Mebane, M. C. Lin, and M. Liu, Chem. Mater. **19**, 1690 (2007).

[22] E. A. Kotomin, Y. Mastrikov, E. Heifets, and J. Maier, PhysChemChemPhys **10**, 4644 (2008).

[23] Y. Choi, M. E. Lynch, M. C. Lin, and M. Liu, J. Phys. Chem. C **113**, 7290 (2009).

[24] E. A. Kotomin, R. A. Evarestov, Y. A. Mastrikov, and J. Maier, PhysChemChemPhys **7**, 2346 (2005).

[25] Y. Mastrikov, E. Heifets, E. Kotomin, and J. Maier, Surf. Sci. **603**, 326 (2009).

[26] L. B. Pankratz, US Bur. Mines Bull. **672**, 509 (1982).

[27] R. A. Robie and B. S. Hemingway, J. Chem. Thermodyn. **17**, 165 (1985).

[28] A. N. Sophie Fritsch, J. Am. Ceram. Soc. **79**, 1761 (1996).

[29] R. Amankwah and C. Pickles, J. Thermal Anal. Calorim. **98**, 849 (2009).

[30] C. Franchini, R. Podloucky, J. Paier, M. Marsman, and G. Kresse, Phys. Rev. B **75**, 195128 (2007).

[31] J. Muscat, A. Wander, and N. Harrison, Chem. Phys. Lett. **342**, 397 (2001).

[32] G. Mallia and N. M. Harrison, Phys. Rev. B **75**, 165201 (2007).

[33] N. C. Wilson, S. P. Russo, J. Muscat, and N. M. Harrison, Phys. Rev. B **72**, 024110 (2005).

[34] F. Cora, M. Alfredsson, G. Mallia, D. S. Middlemiss, W. C. Mackrodt, R. Dovesi, and R. Orlando, *The Performance of Hybrid Density Functionals in Solid State Chemistry*, Structure & Bonding, Vol. 113 (Springer, Berlin, 2004).

[35] G. C. De Fusco, B. Montanari, and N. M. Harrison, Phys. Rev. B **82**, 220404 (2010).

[36] L. Ge, J. H. Jefferson, B. Montanari, N. M. Harrison, D. G. Pettifor, and G. A. D. Briggs, ACS Nano **3**, 1069 (2009).

[37] G. C. De Fusco, L. Pisani, B. Montanari, and N. M. Harrison, Phys. Rev. B **79**, 085201 (2009).

[38] L. Liborio, G. Mallia, and N. Harrison, Phys. Rev. B **79**, 245133 (2009).

[39] C. L. Bailey, L. Liborio, G. Mallia, S. Tomić, and N. M. Harrison, Phys. Rev. B **81**, 205214 (2010).

[40] L. M. Liborio, C. L. Bailey, G. Mallia, S. Tomic, and N. M. Harrison, J. Appl. Phys. **109**, 023519 (2011).

[41] K. Johnston, M. R. Castell, A. T. Paxton, and M. W. Finnis, Phys. Rev. B **70**, 085415 (2004).

[42] [http://webbook.nist.gov/chemistry/].

[43] *CRC Handbook of Chemistry & Physics,* 91st ed. (Taylor & Francis, London, 2010).

[44] D. Kramer and G. Ceder, Chem. Mater. **21**, 3799 (2009).

[45] R. Dovesi *et al.*, CRYSTAL09 User's Manual, Università di Torino, Torino, 2010.

[46] [http://www.crystal.unito.it/basis_sets/ptable.html].

[47] G. Mallia, R. Orlando, M. Llunell, and R. Dovesi, in *Computational Materials Science*, edited by C. Catlow and E. Kotomin, NATO Science Series III: Computer and Systems Science, Vol. 187 (IOS Press, Amsterdam, 2003), pp. 102–121.

[48] C. Pisani, R. Dovesi, and C. Roetti, *Hartree-Fock Ab Initio Treatment of Crystalline Systems*, Lecture Notes in Chemistry, Vol. 48 (Springer-Verlag, Heidelberg, 1988).

[49] E. O. Wollan and W. C. Koehler, Phys. Rev. **100**, 545 (1955).

[50] [http://cds.dl.ac.uk/icsd/].

[51] B. C. Hauback, H. Fjellvïg, and N. Sakai, J. Solid State Chem. **124**, 43 (1996).

[52] N. Hirosaki, S. Ogata, and C. Kocer, J. Alloys Compd. **351**, 31 (2003).

[53] J. E. Post and P. J. Heaney, Am. Mineral. **89**, 969 (2004).

[54] S. Geller, Acta Crystallogr. Sect. B **27**, 821 (1971).

[55] V. Baron, J. Gutzmer, H. Rundlof, and R. Tellgren, Am. Mineral. **83**, 786 (1998).

[56] D. Taylor, Trans. J. Br. Ceram. Soc. **83**, 5 (1984).

[57] A. Bolzan, C. Fong, B. Kennedy, and C. Howard, Austral. J. Chem. **46**, 939 (1993).

[58] X.-F. Wang, Q.-X. Li, X.-Y. Chu, and F. S-H., Chem. J. Chin. Univ. **28**, 821 (2007).

[59] C. R. Ross, D. C. Rubie, and E. Paris, Am. Mineral. **75**, 1249 (1990).

[60] V. Dyakonov *et al.*, Phys. Rev. B **77**, 214428 (2008).

[61] M. Mikami and S. Nakamura, J. Alloys Compd. **408–412**, 687 (2006).

[62] P. R. B. Shirley Turner, Nature (London) **304**, 143 (1983).

[63] D. Balachandran, D. Morgan, G. Ceder, and A. van de Walle, J. Solid State Chem. **173**, 462 (2003).

[64] M. Regulski, R. Przenioslo, I. Sosnowska, D. Hohlwein, and R. Schneider, J. Alloys Compd. **362**, 236 (2004).

[65] S. Mukherjee, A. K. Pal, S. Bhattacharya, and J. Raittila, Phys. Rev. B **74**, 104413 (2006).

[66] R. Tackett, G. Lawes, B. C. Melot, M. Grossman, E. S. Toberer, and R. Seshadri, Phys. Rev. B **76**, 024409 (2007).

[67] T. Suzuki and T. Katsufuji, J. Phys.: Conf. Ser. **150**, 042195 (2009).

[68] W. L. Roth, Phys. Rev. **110**, 1333 (1958).

[69] H. Shaked, J. Faber, and R. L. Hitterman, Phys. Rev. B **38**, 11901 (1988).

[70] M. D. Towler, N. L. Allan, N. M. Harrison, V. R. Saunders, W. C. Mackrodt, and E. Aprà, Phys. Rev. B **50**, 5041 (1994).

[71] K. T. Jacob and M. Attaluri, J. Mater. Chem. **13**, 934 (2003).

[72] L. Wang, T. Maxisch, and G. Ceder, Phys. Rev. B **73**, 195107 (2006).